Urban and Building Science
https://www.sciltp.com/journals/ubs



Article

Check for updates

Toward Personalized Thermal Comfort: A Spatiotemporal Dynamic Heating Strategy for the Catalytic Combustion Local Heater

Hongyue Fang [1,†], Junlong Jiang [1,†], Mingyuan Qin [1,2,*], Xiaofei Han [3], Yindong Yuan [2] and Sijia Sun [4]

[1] School of Architecture and Civil Engineering, Xihua University, Chengdu 610039, China
[2] Department of Mechanical Engineering, Universiti Malaya, Kuala Lumpur 50603, Malaysia
[3] Centre for Building, Construction & Tropical Architecture, Faculty of Built Environment, Universiti Malaya, Kuala Lumpur 50603, Malaysia
[4] Department of Civil Engineering, School of Engineering, Aalto University, 02150 Espoo, Finland
* Correspondence: qinmingyuan@xhu.edu.cn
† These authors contributed equally to this work.

How To Cite: Fang, H.; Jiang, J.; Qin, M.; et al. Toward Personalized Thermal Comfort: A Spatiotemporal Dynamic Heating Strategy for the Catalytic Combustion Local Heater. *Urban and Building Science* **2026**, *2*(3), 1. https://doi.org/10.53941/ubs.2026.100015

Received: 20 February 2026
Revised: 5 April 2026
Accepted: 24 April 2026
Published: 6 May 2026

Abstract: Localized heating can improve thermal comfort in cold environments while reducing energy use relative to whole-space heating; however, robust control remains challenging under rapidly varying outdoor conditions. This study develops an adaptive thermal-comfort prediction model for infrared localized heating to enable personalized spatiotemporal control. A total of 3243 observations were collected from 64 participants using a catalytic-combustion radiant heater, combining subjective thermal votes with multi-site skin-temperature measurements across a range of operating conditions. The results demonstrate that localized heating effectively alleviates cold discomfort, increasing mean skin temperature (MST) by approximately 0.4–1.0 °C. Continuous heating is recommended when the ambient temperature ranges from 0 to 11 °C, as it achieves a thermal satisfaction rate of approximately 65%. Above 11 °C, intermittent operation maintained MST within 30–33 °C and achieved higher satisfaction (around 72%), while reducing the risk of local overheating and improving energy efficiency. To reduce dependence on detailed heat-transfer modeling, five machine learning classifiers were trained and compared; the Random Forest model performed best. After hyperparameter optimization, the model achieved an accuracy of 0.84, F1 scores of 0.83–0.85 across three classes, and AUC values above 0.93, indicating strong discrimination and generalization. These findings provide a foundation for efficient and personalized intelligent control of localized heating in cold outdoor settings.

Keywords: cold environment; personal comfort system (PCS); thermal comfort; infrared localized heating; control strategy; machine learning

1. Introduction

As outdoor activities become increasingly popular, the time people spend in diverse environments continues to expand. Harsh and unpredictable conditions can threaten safety and reduce operational performance [1]. In cold settings, insufficient thermal protection increases the likelihood of hypothermia and other cold-related morbidity. Historical records document numerous incidents; for example, during a US NFL game on 17 January 2024, dozens of spectators required medical treatment for hypothermia [2]. Following the Great East Japan Earthquake on 11 March 2011, 22 people developed hypothermia because of insufficient heating [3]. Many such incidents occur at

Copyright: © 2026 by the authors. This is an open access article under the terms and conditions of the Creative Commons Attribution (CC BY) license (https://creativecommons.org/licenses/by/4.0/).
Publisher's Note: Scilight stays neutral with regard to jurisdictional claims in published maps and institutional affiliations.

outdoor air temperatures between −20 °C and 10 °C [4], often in windy conditions that exacerbate convective heat loss. Rapid atmospheric fluctuations are common in these settings. Evidence from physiology and medicine demonstrates the adverse effects of cold exposure; cold spells have been associated with increased acute myocardial infarction mortality [5]. Local skin temperature decreases more rapidly than it recovers when ambient temperature rises [6]. For the hands, finger temperatures below 20 °C can cause tissue damage and reduce manual dexterity [7]. Cold exposure can also impair psychological and behavioral functioning by weakening memory and alertness, slowing reaction time, and compromising decision-making [8]. Overall, cold environments present intertwined physiological and cognitive risks. Conventional whole-space heating is often ill-suited to dynamic outdoor contexts because it responds slowly to changing comfort needs and can result in redundant coverage and high energy use. As the world advances toward the United Nations 2030 Sustainable Development Goals, global resource consumption is projected to increase substantially, reinforcing the need for energy conservation and emissions mitigation. Localized heating technologies that adapt to individual needs and environmental variability can therefore maintain comfort and safety in cold conditions while reducing energy waste and improving efficiency. From the perspective of urban and building science, improving the thermal comfort of public spaces such as stadiums, lounges, and shelters plays an important role in enhancing urban resilience [9]. In addition, replacing whole-space heating with localized heating provides a new pathway for improving building energy efficiency.

1.1. Local Heating and Thermal Comfort

The principal advantage of localized heating devices is their ability to maintain thermal comfort and health while improving energy efficiency by directing heat to the occupied body region. Targeted heating is typically delivered through three heat-transfer mechanisms: conduction, convection, and radiation. Thermal conduction transfers energy via direct physical contact between surfaces. For example, Liu et al. [10] used heating pads to warm multiple body regions and found heating the waist produced the greatest improvement in overall thermal perception, whereas heating the knees and chest had smallest effect. Wang et al. [11] designed full-body heated garments based on conduction, enhancing comfort while providing sustained and controllable warming of different body regions. Thermal convection relies on heat exchange between a fluid medium and the body surface. Studies on personalized ventilation show that heating localized airflow to 26 °C in a 20 °C environment improves local thermal sensation [12]. Du et al. [13] assessed convective heating for the feet and lower body in cold settings, noting that temperatures below 12–14 °C increased mean skin temperature and thermal sensation votes. In contrast, thermal radiation transmits energy directionally without a transport medium. Radiant leg warmers have been used to improve winter thermal comfort for office workers [14], and radiant phase-change floor heating has been examined for its effects on comfort and energy use [15]. Each approach nevertheless faces challenges in dynamic outdoor environments in terms of endurance, comfort, and thermal efficiency. Conduction-based systems often rely on limited battery capacity, which restricts operating duration [16,17]. Convective heating can cause discomfort due to strong airflow and may suffer from rapid heat dissipation, reducing efficiency [12]. Radiant heating can deliver effective comfort at low ambient temperatures and supports intermittent operation [4], which helps conserve energy. These attributes make radiant heating a promising option for localized heating in cold outdoor settings. Accordingly, this study employs an infrared radiant heater and examines the thermal response characteristics of localized heating under cold outdoor conditions.

1.2. Predictive Models

Human thermal comfort is influenced not only by air temperature but also by multiple interrelated factors, including relative humidity, air velocity, radiant temperature, metabolic rate, and clothing insulation [18]. In dynamic outdoor environments, these parameters vary nonlinearly, complicating thermal state prediction and control. Robust models are therefore needed to quantify and anticipate thermal state under realistic operating conditions. Figure 1 summarizes reported prediction accuracies of common algorithms for key thermal comfort indices and their associated input variables, focusing on Overall Thermal Sensation Vote (OTSV), Overall Thermal Comfort Vote (OTCV), and Thermal Preference Vote (TPV). The pathways associated with OTCV are particularly dispersed, indicating strong nonlinear relationships with environmental, physiological, and behavioral variables. TPV reflects individual preference and is inherently subjective. Existing studies predominantly employ machine learning methods, including Support Vector Machines (SVM), Decision Trees (DT), Random Forests (RF), Artificial Neural Networks (ANN), K-Nearest Neighbors (KNN), and Logistic Regression (LR), with predictors represented as either categorical or continuous variables. High predictive performance has been reported; for example, Choi and Yeom [19] achieved 94.39% accuracy for OTSV using DT, and Yang et al. [20] reported 95.80% accuracy for OTSV, OTCV, and TPV using SVM, DT, and KNN. Nevertheless, the choice of input

variables remains critical, for instance, Zhou et al. [21] incorporated subjective evaluations and device states as predictors in an SVM model for OTSV. Personalized control of localized heating relies on temporal descriptors (e.g., thermal history and duration), spatial descriptors (e.g., heated body zones and environmental gradients), and subjective factors (e.g., user adjustments). Imbalances among these components can lead to model overfitting or underfitting. The ultimate aim of accurate prediction is to support effective control. Data-driven approaches have begun to establish regulatory frameworks that balance comfort and energy efficiency. Cai et al. [22] combined machine learning with a modified PMVst model within a data-integrated framework, and Huang et al. [23] proposed a data-driven framework for thermal preference prediction using algorithms such as LightGBM, XGBoost, RF, and DT. These frameworks directly connect thermal comfort prediction with heating control. To accommodate the multidimensional influences specific to infrared localized heating, dedicated strategy frameworks and models are still required. Accordingly, this paper develops an adaptive thermal comfort prediction framework for catalytic-combustion radiant heating that explicitly integrates temporal, spatial, and subjective variables.

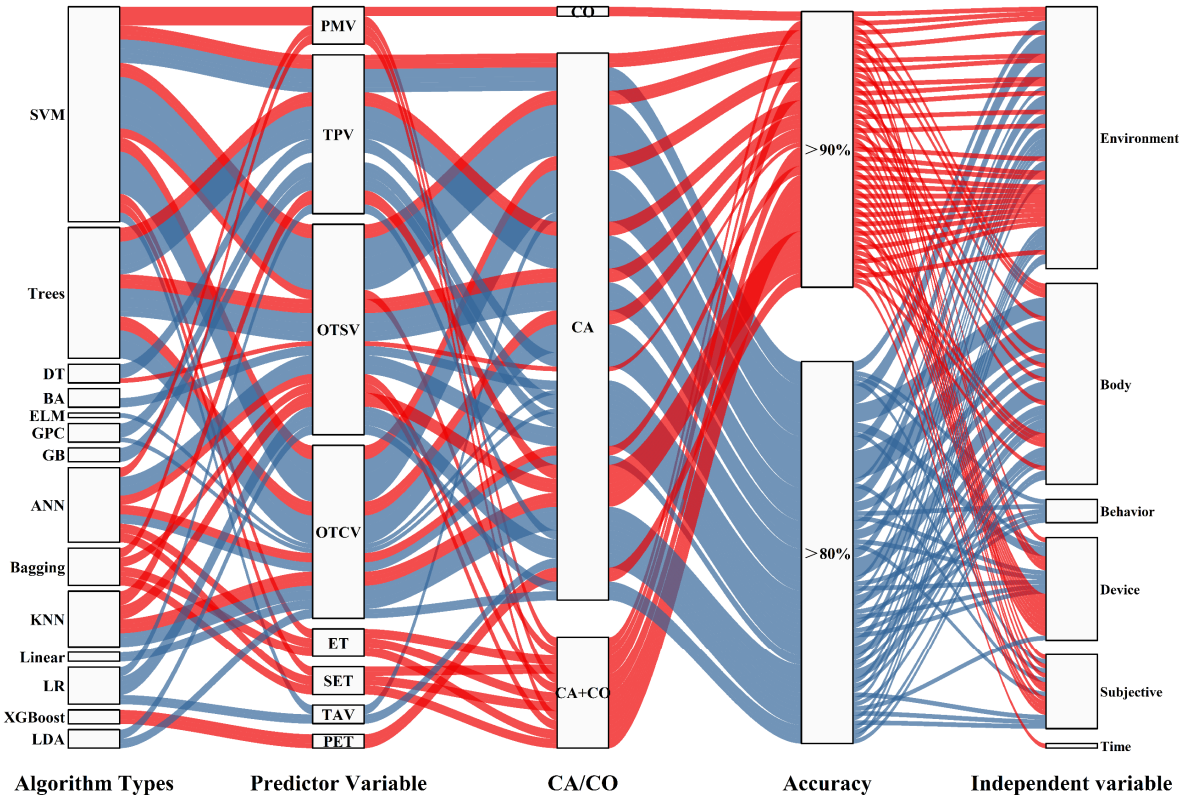


Figure 1. Sankey diagram summarizing recent machine-learning studies on thermal comfort prediction.

1.3. Research Gaps and Content

Based on the foregoing analysis, existing studies on local personal thermal comfort prediction and heating strategy development have been largely established under quasi-steady environmental conditions. As a result, they remain limited in their ability to capture the spatiotemporal interactions between localized heating and subjective human thermal responses in dynamic environments. This limitation is particularly critical in cold outdoor open spaces, where continuous fluctuations in air temperature, humidity, and wind speed create highly non-stationary thermal conditions. Under such circumstances, conventional control frameworks derived from classical heat transfer equations and prescribed physical boundary conditions are insufficient to represent the time-lagged, nonlinear, and inter-individual characteristics of subjective thermal sensation. In addition, for infrared radiant localized heating scenarios, adaptive prediction and control approaches that can integrate multidimensional information, including device operation, spatial position, exposure duration, environmental conditions, and physiological and psychological responses, are still lacking.

To address these gaps, this study developed a data-driven adaptive framework for infrared localized heating based on 3243 sets of experimental observations. The framework integrates spatiotemporal variables related to thermal history, operating time, heating distance, environmental conditions, and physiological responses, and builds upon our previous strategy framework established under fixed operating conditions and dimensionless heat transfer parameters. By replacing complex mechanistic heat transfer modelling with a data-driven approach, the

proposed framework is able to capture the nonlinear and time-dependent characteristics of human thermal comfort responses more effectively. Furthermore, five commonly used machine-learning algorithms were systematically evaluated to identify a robust model for OTSV prediction, and key hyperparameters were optimized to further enhance predictive performance. The results provide empirical support for the intelligent prediction and dynamic control of personalized radiant heating systems.

2. Materials and Methods

This section summarizes the methodology of the previously conducted experiments from which the data used in this study were derived, including the controlled environment and the procedures for collecting participants' subjective thermal evaluations. Rather than reporting a newly conducted human-subject experiment, the present study is based on the integration and secondary analysis of an existing experimental data set. Experiments under multiple temperature and operating conditions yielded 3243 valid samples, including PCS operation, key environmental parameters, and participants' thermal perceptions. These data were then used to refine the heating strategy framework originally developed under fixed operating conditions and to train machine learning models for predicting OTSV. Five widely used algorithms with relatively lightweight model structures were evaluated.

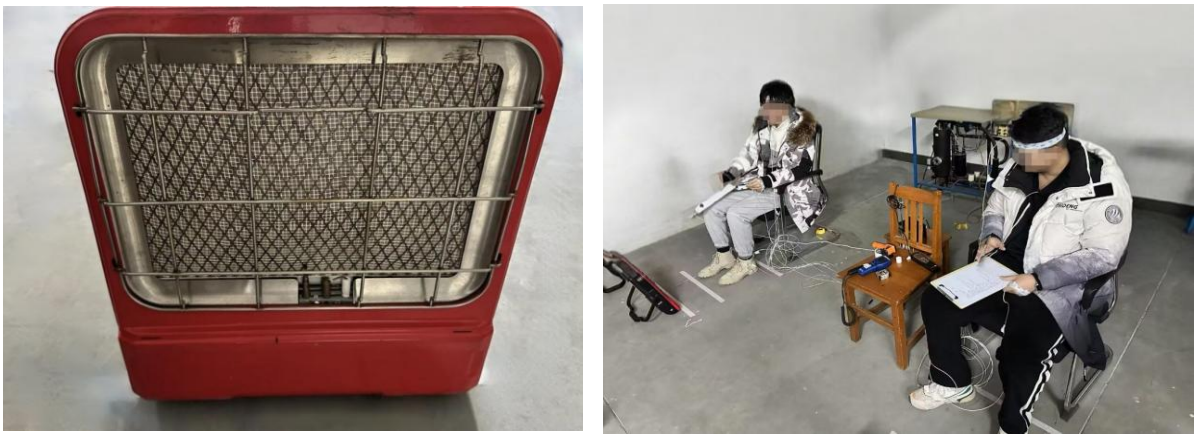
2.1. Experimental Setup

2.1.1. Created Environment

This study employed a natural diffusion catalytic oxidation gas infrared radiant heater (HC) as the experimental heating device to simulate a representative form of individual radiant heating in cold open environments where a stable electricity supply is unavailable. Conventional electric localized heating devices are often constrained by power availability and limited environmental adaptability. Meanwhile, traditional combustion-based heating technologies generally suffer from inadequate combustion, an open flame, and unstable local heat output. In contrast, catalytic combustion heaters offer a relatively clean combustion process, lower radiant surface temperatures, and stable flameless radiant heat output, making them a more suitable potential heat source for such applications.

The heater's design features an effective radiating surface of approximately 250 mm × 200 mm, constructed from a non-metallic Al_2O_3 substrate coated with a precious metal Pt catalyst layer, which facilitates stable flameless infrared radiation emission. Under stable gas delivery (fuel supply rate of 1 L/min) and natural oxygen diffusion, the radiating surface maintains an average temperature of about 409 °C. Under natural convection at an ambient temperature of 20 °C, the radiant power of the HC was 515 W, while the energy consumption with butane fuel was approximately 2778 kJ/h. To prevent wind-induced variations in oxygen supply—which could affect catalytic efficiency, surface temperature, and radiation stability—the heater's gas flow was fixed at 1 L/min and positioned on the leeward side under windy conditions. This placement minimizes performance disturbances caused by oxygen-enriched combustion on the windward side. The heater's appearance is shown in Figure 2a, and its detailed structure and operating principles are described in reference [4].

All experimental conditions were designed to simulate localized radiant heating scenarios in cold outdoor environments. The calf, particularly the shin, was defined as the core heating zone because of its high sensitivity to cold [24]. The ambient temperature range for the study was set between −10 °C and 16 °C. The upper limit aligns with the minimum heating temperature specified in GB/T 18883-2022 [25], while the lower limit was determined based on physiological tolerance and safety considerations. Temperature was monitored using a Qingping Air Detector CGS1 (measurement range: 10–50 °C, accuracy: ±0.8 °C). Two primary operating modes were tested: intermittent heating (C_1) and continuous heating (C_2). These modes simulate common usage patterns in real-world settings. The intermittent mode, with varied on-off cycles (5–15 min), represents short-duration outdoor exposure or energy-efficient operation strategies. The continuous mode was used to assess responses under stable radiant conditions. To examine the effect of heating distance (spatial strategy) on local thermal sensation and exposure, three heating distances were established: 40 cm, 60 cm, and 80 cm [26]. Wind speed and relative humidity were set according to actual field measurements, with ranges of 0.01–1.43 m/s and 12–78%, respectively. These ranges encompass typical outdoor conditions, including low and high wind speeds under dry and humid scenarios. To isolate the effect of the radiant heating system, the experiment was conducted in a controlled setting where the building envelope was sealed. This precaution prevented interference from factors such as open doors, solar radiation, and heat transfer from adjacent structures. A view of the prepared experimental site is provided in Figure 2b.



(**a**) (**b**)

Figure 2. Catalytic combustion heater and experimental site. (**a**) The heater's appearance; (**b**) The prepared experimental site.

Environmental parameters were measured according to the method recommended by ASHRAE Standard 55-2023 [27]. Sensors were placed at heights of 0.1 m, 0.6 m, and 1.1 m above the floor to represent conditions at the ankle, waist, and head levels of a standing person. To prevent measurement errors caused by direct radiant heating or optical interference from the heaters, all sensor surfaces were shielded with perforated aluminum foil. This allowed sufficient air exchange while ensuring measurement accuracy. Given the extended duration of the experiments and full exposure to natural environmental fluctuations, some parameters varied within their predetermined ranges. However, all conditions successfully met the preset experimental criteria. The specific parameter combinations and their statistical results are provided in Table 1.

Table 1. Experimental conditions for continuous and intermittent heating cases.

Cases	Heating Method	T_{in} (°C)	RH (%)	Wind (m/s)	Heating Distance (cm)	Heating Time (min)	Intermittent Time (min)	Experiment Time (min)
Case 1−1	Intermittent (C_1)	11	69.2	0.02	40	5	5	60
Case 1−2		12	67.2	0.02	40	10	15	75
Case 1−3		12	67.5	0.02	40	15	10	75
Case 2−1		12	68.9	0.02	60	5	15	60
Case 2−2		12	67.3	0.02	60	10	10	60
Case 2−3		13	67.9	0.02	60	15	5	60
Case 3−1		13	66.9	0.02	80	5	10	60
Case 3−2		13	67.5	0.02	80	10	5	60
Case 3−3		13	66.0	0.02	80	15	5	60
Case 4−1	Continuous (C_2)	−10	14.5	1.43	60	60	-	60
Case 4−2		−5	20.1	1.43	60	60	-	60
Case 4−3		0	29.0	1.43	60	60	-	60
Case 4−4		5	24.5	0.03	60	60	-	60
Case 4−5		8	24.5	0.03	60	60	-	60
Case 4−6		11	24.5	0.02	60	60	-	60
Case 4−7		15	24.5	0.01	60	60	-	60
Case 5−1		12	57.8	0.02	40	60	-	60
Case 5−2		12	56.7	0.02	60	60	-	60
Case 5−3		12	55.8	0.02	80	60	-	60

2.1.2. Physiological Parameters and Psychological Feedback

Sixty-four volunteers (32 males, 32 females) participated in the experiments. Their basic information was collected, including age (24.0 ± 2.7 years), height (168.8 ± 8.0 cm), weight (64.4 ± 13.2 kg), and calculated Body Mass Index (BMI) (22.46 ± 3.61 kg/m²). The thermal insulation of their clothing was 2.13 ± 0.71 clo, determined according to ASHRAE Standard 55-2023 [27]. To minimize variations in thermal expectations between participants and to avoid physiological biases, all volunteers confirmed that they were healthy and non-smokers. They were also instructed to avoid consuming stimulating foods for 12 h before the test and to refrain from eating or drinking during the test.

During the experiments, participants' skin temperature was measured with water bath-calibrated PT100 thermocouples and recorded in real-time by a multichannel data logger (QZXJY-24CH-1, Beijing Qingzheng

Fenhao Technology Co., Ltd, Beijing, China). The measurement points included the forehead, chest, arm, hand, thigh, shin, and foot. These data were used to calculate the mean skin temperature (MST) using weighting coefficients based on the skin surface area weighting factors for Asian populations [28]:

$$MST=0.073T_{forehead}+0.373T_{chest}+0.14T_{arm}+0.052T_{hand}+0.15T_{thigh}+0.135T_{shin}+0.074T_{foot} \quad (1)$$

Subjective thermal evaluations were collected via questionnaires, which recorded both overall and local thermal evaluation. Thermal sensation was assessed using a standard 7-point scale (Cold (−3), Cool (−2), Slightly cool (−1), Neutral (0), Slightly warm (1), Warm (2), Hot (3)) [29]. Thermal comfort was evaluated on an asymmetric 5-point scale consisting of Extremely uncomfortable (−4), Very uncomfortable (−3), Uncomfortable (−2), Slightly uncomfortable (−1), and Comfortable (0) [30]. Questionnaires were administered at fixed intervals: every 10 min during continuous heating and every 5 min during intermittent heating. Participants also provided feedback immediately before any adjustment to heater operation status or heating distance. In total, 3243 valid questionnaire responses were collected, providing the dataset foundation for developing the intelligent personalized thermal comfort prediction model in this study.

2.1.3. Experimental Procedure

The experiment consisted of four main phases. Phase A: Preparation. Before entering the test chamber, subjects had their height and weight measured. Thermocouples were then applied to seven designated body sites. Phase B: Cold Exposure and Adaptation. Subjects remained seated and avoided unnecessary movement. A 15-min adaptation period was implemented to minimize the influence of prior thermal history, after which subjects completed an initial questionnaire. Phase C: Heating. According to the conditions in Table 1, stabilized HC units positioned according to the predefined experimental configurations. Ambient and skin temperatures were recorded continuously. In the intermittent heating group (C_1), subjects completed questionnaires every five minutes, with heating adjustments made only after each questionnaire. In the continuous heating group (C_2), subjects received uninterrupted heating and completed questionnaires every ten minutes. Phase D: Conclusion. The thermocouples were removed from the subjects, who then exited the experimental chamber.

2.2. Intelligent Strategies and Models

2.2.1. Strategic Framework

The research team previously established a framework for regulating heating in wind-cooled environments [31]. This framework uses empirical heat transfer formulas to estimate local convective heat loss from the human body under fixed environmental parameters and assumptions, thereby enabling thermal compensation for localized thermal discomfort. The control logic within this framework balances three factors: individual thermal comfort needs, energy consumption limits, and the combustion and emission characteristics of the heater. A key operational parameter is the gas flow rate, which has a control threshold of 0.6 L/min. Exceeding this rate ensures combustion efficiency above 99%, while falling below it leads to increased emissions from incomplete combustion. When the human body is overheated (current OTSV > 0) and the flow rate falls below this threshold, the heater is recommended to be turned off to prevent overheating and unnecessary energy consumption. Conversely, when the body is overcooled (current OTSV < −1), the required heat input is quantified using dimensionless coefficients such as the Nusselt number, and the gas flow rate is increased accordingly.

While the existing framework effectively manages energy use, emissions, and basic comfort in steady conditions, it falls short in dynamic settings for two reasons: (i) heat loss calculations rely on fixed or quasi-steady-state assumptions, making it difficult to capture the temporal hysteresis and non-linear response of human thermal sensation; (ii) this computational model struggles to account for individual variations in thermal perception, thereby limiting its general applicability. To overcome these boundary condition limitations, this study refines the method for determining thermal demand while preserving the original logical structure. The proposed approach reduces reliance on physical modeling of localized heat transfer mechanisms and instead emphasizes the data-driven mapping between multidimensional environmental conditions and subjective thermal responses. This enables rapid prediction and regulation of the human body's overall thermal state, as illustrated in Figure 3.

In the proposed framework, the machine-learning model is incorporated as a data-driven substitute for the thermal state identification component in the original rule-based framework, thereby supporting real-time heating decision-making. Specifically, the model predicts the subject's current OTSV from environmental parameters, device operating conditions, spatiotemporal variables, and human-related information that can be acquired in real time. The predicted OTSV is then compared with the predefined target OTSV or comfort threshold to determine whether the heating intensity should be adjusted or the operating mode should be switched. In this manner, the

model optimizes the thermal demand identification process while preserving the original framework constraints and operational boundaries, thereby improving the responsiveness and practical applicability of the framework under dynamic environmental conditions.

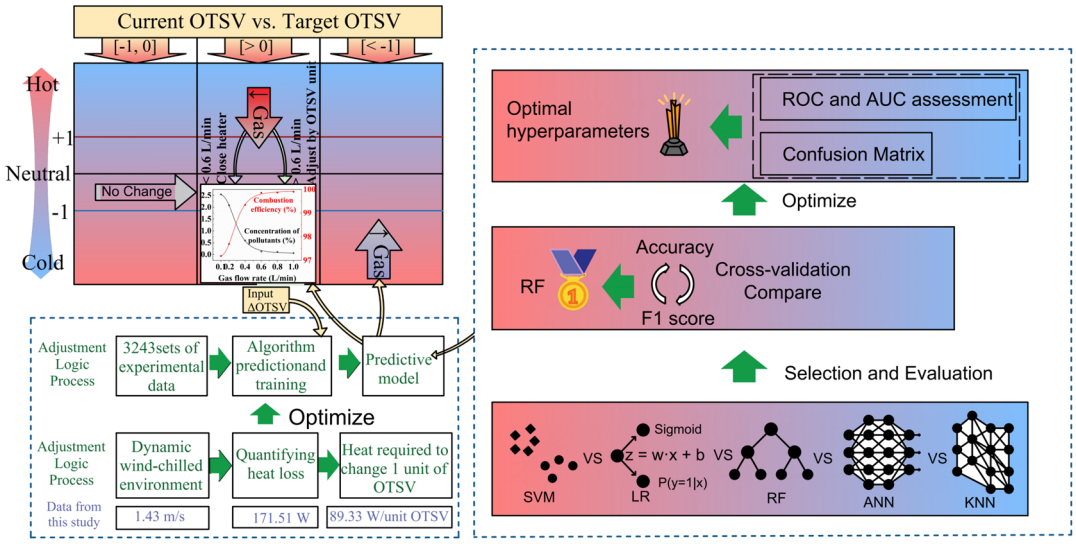


Figure 3. Control strategy for the catalytic combustion heater considering personal thermal sensation, energy savings, and emissions.

2.2.2. Variable Selection and Dimension Reduction

The input variables for this study comprise a multidimensional feature set, encompassing five major categories: infrared radiation equipment parameters, spatial parameters, temporal parameters, environmental parameters, and human physiological and psychological characteristics. The specific variables within these categories are as follows. The temporal dimension includes thermal history (His_{heat}) and the current time point (t) relative to the global time scale, which is used to investigate the temporal dynamics of thermal sensation under intermittent heating patterns with varying start-stop rhythms; Spatial distance (D_{heat}) evaluates localized and overall thermal comfort at varying distances between the heater and the human body; Infrared radiation equipment parameters include heat source area (A_{heat}), emission wavelength (Wave), heat source temperature (T_{heat}), and switch status (Status); Psychological parameters collected via subjective questionnaires include Overall Thermal Sensation Vote (OTSV) and Local Thermal Sensation Vote (LTSV); Human information and physiological parameters: clothing thermal resistance (Clo), local skin temperatures at seven body locations, and mean skin temperature (MST); Environmental parameters: real-time recorded ambient temperature (T_{in}), relative humidity (RH), and wind speed under various operating conditions.

In addition, while a large data sample size can enhance the accuracy and comprehensiveness of machine learning algorithms in feature learning, selecting well characterized input variables can simplify algorithm training, shorten training duration, and enhance model interpretability. Therefore, it is imperative to investigate potential interactions among variables, stemming from mutual influence, before finalizing the input variables. By conducting correlation analysis, the degree of association among the variables can be established, thereby aiding in the removal of unnecessary input variables.

Figure 4 illustrates the correlation results among the various input variables. Where the oval slopes to the right represent a positive correlation, the rounder the shape represents a smaller correlation coefficient, and the darker the color represents a correlation coefficient closer to ±1, and vice versa. A strong negative correlation between T_{heat} and Wave is evident, as dictated by Planck's law. Additionally, subjective thermal sensation voting exhibits a strong correlation between overall and localized responses. All localized body positions display a strong positive correlation. Consequently, to avoid multicollinearity, the local thermal sensation variables were excluded from the model, and OTSV was retained as the sole output indicator. The model outputs the predicted OTSV at the current moment, which is subsequently compared with the predefined target OTSV to inform heating strategy adjustment. Despite the limited positive correlation among few body locations for skin temperature, MST was derived by weighting the human body's local surface area. Thus, this linear relationship was disregarded, and only MST was maintained as a characterizing variable. In summary, the model's final input variables are His_{heat}, t, D_{heat}, A_{heat}, T_{heat}, Status, Clo, T_{in}, RH, and Wind. The only output variable is OTSV.

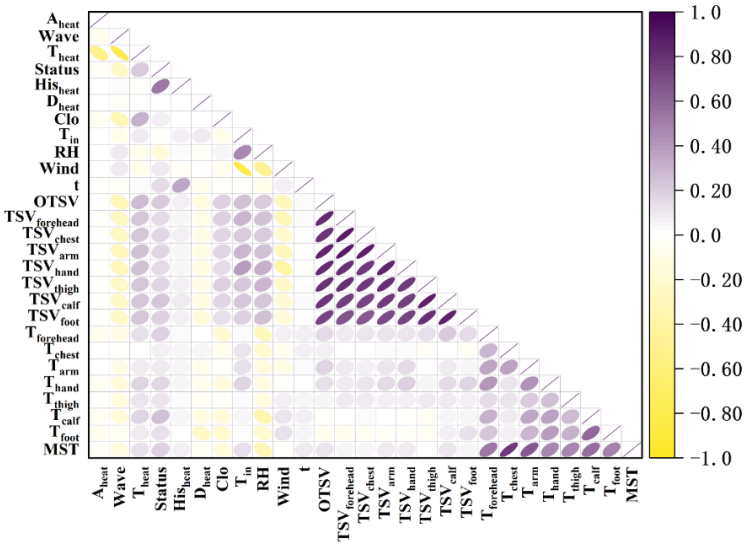


Figure 4. Results of correlation analysis between input variables.

2.2.3. Model

Following the variable screening analysis in Section 2.2.2, OTSV was selected as the target variable for model prediction. Although the original OTSV scale consists of seven discrete levels, as shown in Figure 1, most previous studies on subjective thermal modeling have treated OTSV as a categorical rather than a continuous regression variable. Accordingly, this study recategorized the original OTSV data into three classes consistent with the operational framework: OTSV < −1 is recorded as "overcooling", OTSV = [−1–0] as "neutral", and OTSV > 0 as "overheating", and are respectively encoded as 0, 1, and 2 to meet the input requirements of machine learning classification models. On this basis, data preprocessing was conducted on all raw data. First, the limited number of missing values and outliers in the dataset were handled using iterative imputation or removal followed by iterative imputation. Next, given that differences in the physical properties and scales of input variables could interfere with model training, numerical features were standardized using the StandardScaler method. To ensure the reliability of model training and performance evaluation, the preprocessed dataset was randomly split into training and testing sets in a 7:3 ratio. Furthermore, to reduce uncertainty from random splitting and improve model generalization, five-fold cross-validation was applied to the training set.

After data preprocessing, suitable machine learning algorithms for the prediction task were identified. Algorithm selection was guided by their prevalence and practical validation in prior thermal comfort research. As illustrated in Figure 1, LR, KNN, RF, SVM, and ANN are notably more prevalent in related thermal comfort prediction studies than other algorithms. This study selected these five algorithms and defined their hyperparameter matrices, as shown in Table 2.

Table 2. Hyperparameter settings for each algorithm.

Model	Hyperparameter	Description	Search Range or Values
LR	C	Regularization strength	2^{-10}–2^{10} (15 values, log scale)
	solver	Optimization solver	newton-cg, lbfgs, liblinear, sag, saga
	multi_class	Multi-class strategy	one-vs-rest (OVR)
KNN	n_neighbors	Number of neighbors	2–10
	metric	Distance metric	euclidean, manhattan, chebyshev
SVM	C	Regularization parameter	2^{-10}–2^{10} (15 values, log scale)
	γ	Kernel coefficient	2^{-10}–2^{10} (15 values, log scale)
	kernel	Kernel function	Radial basis function (rbf)
RF	n_estimators	Number of trees	50–500 (step = 50)
	max_depth	Maximum tree depth	2–19
	min_samples_split	Minimum samples to split a node	2, 3, 4
	min_samples_leaf	Minimum samples per leaf	1, 2, 3
ANN	hidden_layer_sizes	Network architecture	n × L, where L = {4, 8, 16, 32, 64} and n = {50, 100, 150}
	activation	Activation function	identity, logistic, tanh, relu
	solver	Optimization algorithm	SGD, Adam, LBFGS
	α	L2 regularization coefficient	0.0001, 0.001, 0.01, 0.1
	learning_rate	Learning rate schedule	invscaling (fixed)

Model performance was comprehensively evaluated using multiple metrics. These include Accuracy (ACC), Precision (PR), Recall (RE), the F1 score, and the Receiver Operating Characteristic (ROC) curve with its Area Under the Curve (AUC), all computed based on the confusion matrix. Accuracy, Precision, Recall, and the F1 Score assess classification performance for individual categories, while AUC evaluates the model's overall ability to discriminate between classes across different classification thresholds. Accuracy (ACC) measures the proportion of correctly classified samples in the entire dataset. Recall (RE) measures the proportion of actual positive samples that are correctly identified. Precision (PR) indicates the proportion of predicted positive samples that are actually positive, reflecting the model's reliability in positive prediction. These metrics are calculated using Equations (2)–(4) [32]:

$$\text{Accuracy} = \frac{TP + TN}{TP + TN + FP + FN} \tag{2}$$

$$\text{Recall} = \frac{TP}{TP + FN} \tag{3}$$

$$\text{Precision} = \frac{TP}{TP + FP} \tag{4}$$

where True Positives (TP) and True Negatives (TN) represent the number of samples that are correctly identified as positive and negative, respectively. In contrast, False Positives (FP) are negative samples incorrectly classified as positive, and False Negatives (FN) are positive samples incorrectly classified as negative.

The F1 score provides a more balanced assessment of a model's overall classification performance, especially when class distributions are imbalanced. It ranges from 0 to 1, with values closer to 1 indicating superior classification performance. Due to the disparity in sample sizes across categories, this study also reports classification metrics for each individual category. The formula for its calculation is given in Equation (5) [33]:

$$F1 = 2 \times \frac{PR \times RE}{PR + RE} \tag{5}$$

Furthermore, the Receiver Operating Characteristic (ROC) curve is used to evaluate a model's discriminative ability by plotting the relationship between the True Positive Rate (TPR) and the False Positive Rate (FPR) across different classification thresholds. The Area Under the Curve (AUC) quantifies the area under the ROC curve and ranges from 0 to 1. An AUC value approaching 1 indicates strong model discrimination between categories. Conversely, When the AUC is ≤ 0.5, it indicates that the model's predictions are equivalent to random guessing or that the model has failed to learn meaningful class distinctions.

3. Results and Discussion

3.1. Skin Temperature Response Characteristics

Skin temperature is a key physiological indicator of human thermal response and shows significant dynamic correlations with heating duration, distance, and environmental conditions. The shin, being the area directly exposed to radiant heating, serves as one of the most representative sites for analyzing localized skin temperature changes. As shown in Figure 5, when the heater is activated, the temperature at this site rises rapidly before gradually stabilizing. Lower ambient temperatures result in slower rates of increase and lower final stable temperatures. Specifically, in Case 4−(1−3) (T_{in} < 0 °C), the average shin temperature stabilized at 29 °C, 31 °C, and 31.5 °C, respectively. In contrast, in Case 4−(4−7) (T_{in} = 5 °C–15 °C), shin temperatures were generally maintained at or above 33 °C. This clearly demonstrates the differential impact of ambient temperature on local thermal response. Further examination of Figure 6 reveals that under continuous heating modes (Case 4−(1−7), Case 5−(1−3)), heating duration exhibits a strong positive correlation with MST, which increases over time. Under intermittent heating, MST exhibits periodic fluctuations synchronized with the "heat-pause" cycle while remaining within a relatively stable range of 30–33 °C. This indicates that intermittent heating can maintain healthy skin temperatures while reducing energy consumption. The stabilized MST values in Case 5−(1−3) decreased with increasing heating distance: 33.2 °C at 40 cm, 33.0 °C at 60 cm, and 32.8 °C at 80 cm. This suggests that shorter heating distances produce higher radiant heat flux density, resulting in greater increases in skin temperature [4]. Notably, although heating is applied locally to the shin and typically does not cause significant changes at other body sites, overall MST still increases by 0.5–1.0 °C. This demonstrates that localized heating can effectively improve the body's overall physiological thermal state. Specifically, in the Case 5 series (T_{in} = 12 °C), both local skin temperature and MST remained around 33 °C, consistent with the range reported by Li et al. (upper limit

ranging from 30.4 °C to 34.1 °C) [34]. These results confirm that optimizing heating mode and distance can maintain skin temperature within a comfortable range under cold conditions, demonstrating the effectiveness and practical applicability of the personalized localized heating strategy.

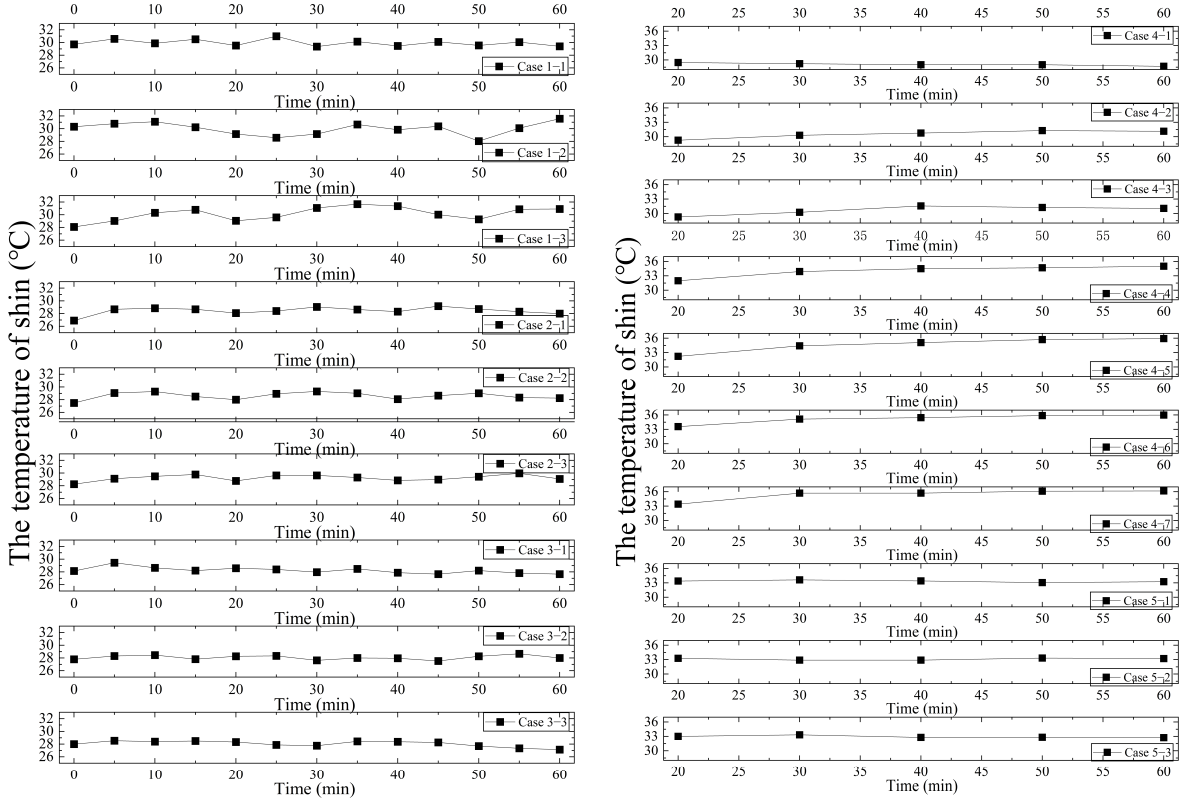


Figure 5. Average shin temperature under different operating conditions.

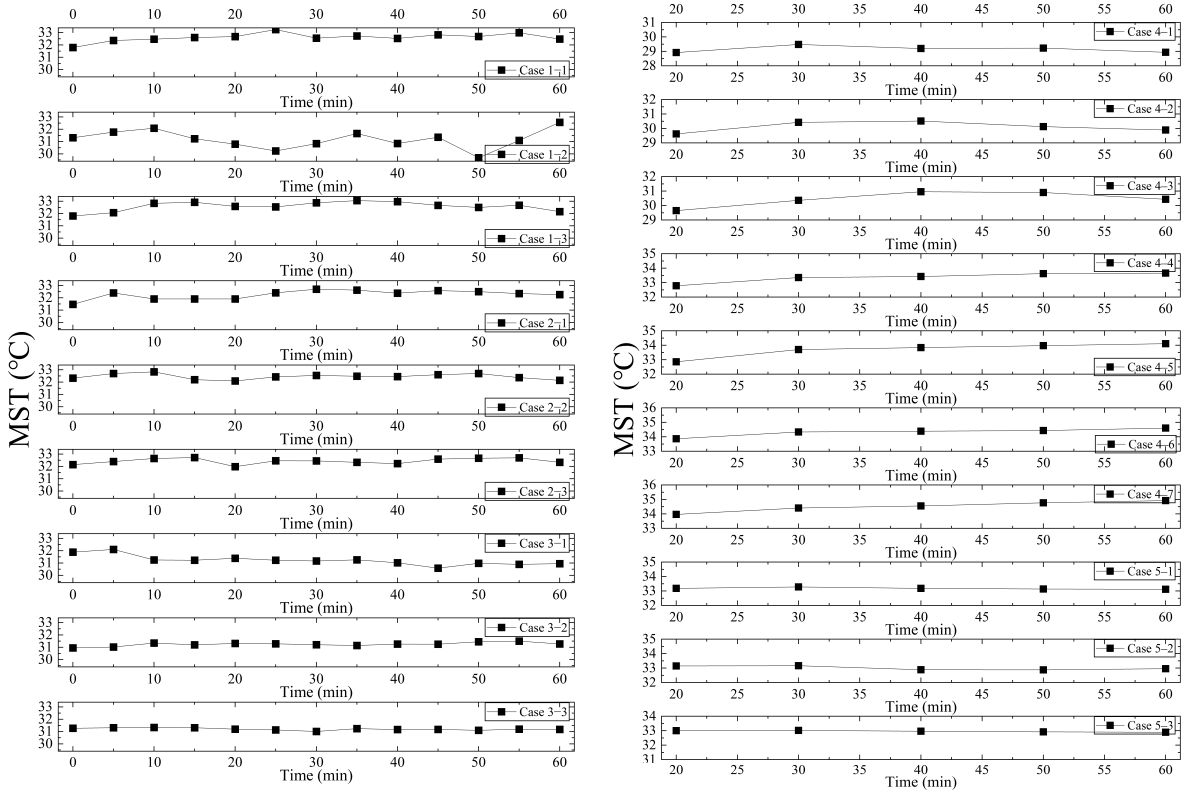
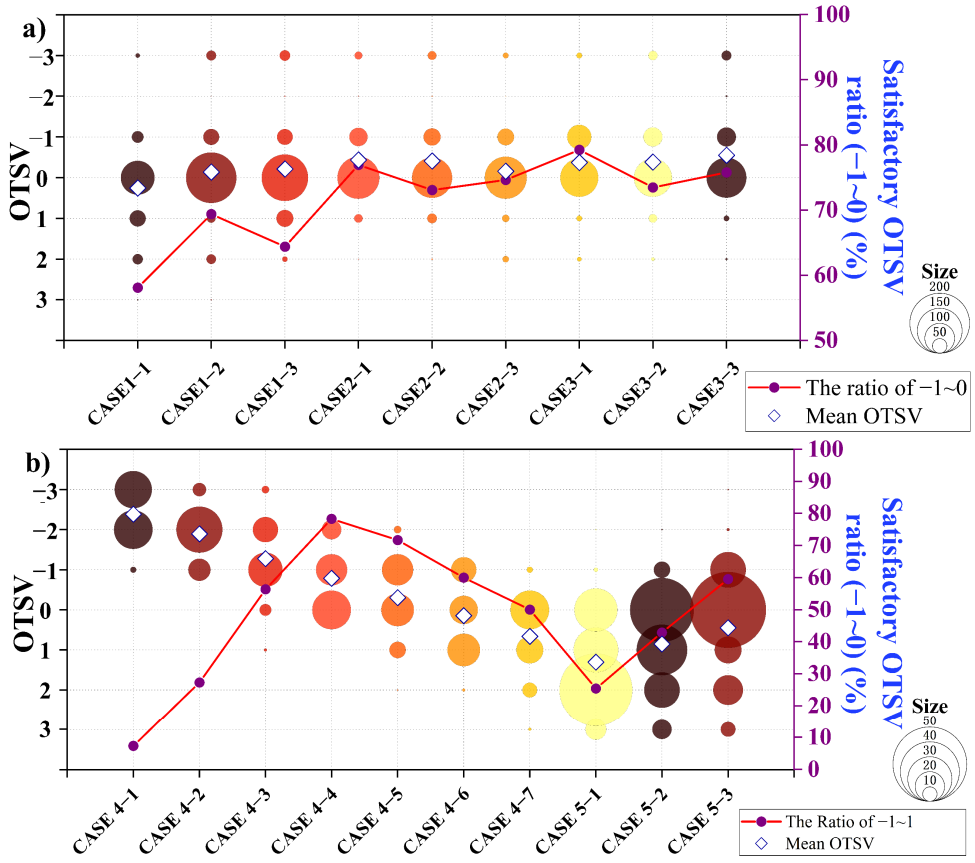


Figure 6. MST under different operating conditions.

3.2. Subjective Thermal Evaluation

Based on the framework established in Section 2.2.1, this study defines the target regulatory state in cold environments as an OTSV within [−1,0] (corresponding to 'slightly cool' to 'neutral'). Figure 7 illustrates subjective thermal satisfaction across different scenarios, where OTSV and OTCV values between −1 and 0 are used as the criterion for 'satisfaction'. The circle size represents the frequency of each rating, while dashed lines indicate the proportion of satisfied responses. Diamonds and hexagons represent the mean OTSV and OTCV values, respectively. Figure 7a,c show the intermittent heating phase (T_{in} > 11 °C), where OTSV satisfaction remained consistently above 60%, with an average of 72%. During this phase, the most frequent OTSV and OTCV ratings clustered near zero, with mean OTSV ranging from 0 to 1 and mean OTCV from −1 to 0. This indicates that most subjects experienced neutral thermal conditions and reported high thermal satisfaction under this heating mode. It should be noted that the proportion of OTSV values within [−1,0] did not increase further, primarily because some subjects' ratings shifted toward 'overheating' rather than insufficient heating, indicating excessive local heating intensity under this mode. For instance, in the Case 1 series (40 cm), OTSV satisfaction was below 70%, whereas OTCV satisfaction exceeded 90%. This suggests that slightly warm conditions may enhance thermal pleasure in cold environments. In contrast, OTSV satisfaction exceeded 73% in the Case 2 and Case 3 series, showing that the long-distance intermittent heating strategy can maintain thermal comfort while saving energy. Figure 7b,d show that in the continuously heated Case 4 series (fixed 60 cm), the average OTSV satisfaction increased to 65% when T_{in} exceeded 0 °C (Case 4−(3−7)). As T_{in} increased from −10 °C to 15 °C, the most frequent OTSV and OTCV ratings shifted from the cold range (−3 to −2) to the target interval of −1 to 0 and stabilized. At the same ambient temperature (12 °C), comparisons within the Case 5 series show that for Case 5−1 (40 cm), the most frequent ratings were concentrated between +1 and +2, with average OTSV satisfaction below 30%, whereas in Case 5−3 (80 cm), the ratings clustered within the target range of −1 to 0, achieving 60% average OTSV satisfaction. Furthermore, OTSV and OTCV satisfaction exhibited consistent trends, with OTCV satisfaction consistently exceeding 90%. However, OTSV satisfaction was relatively lower and increased with greater heating distance. This indicates that appropriately increasing the heating distance can reduce local overheating and improve the alignment between thermal sensation and comfort evaluation. These findings suggest that adjusting heating intensity or operational strategies is necessary to prevent local overheating and further enhance overall thermal comfort in practice.



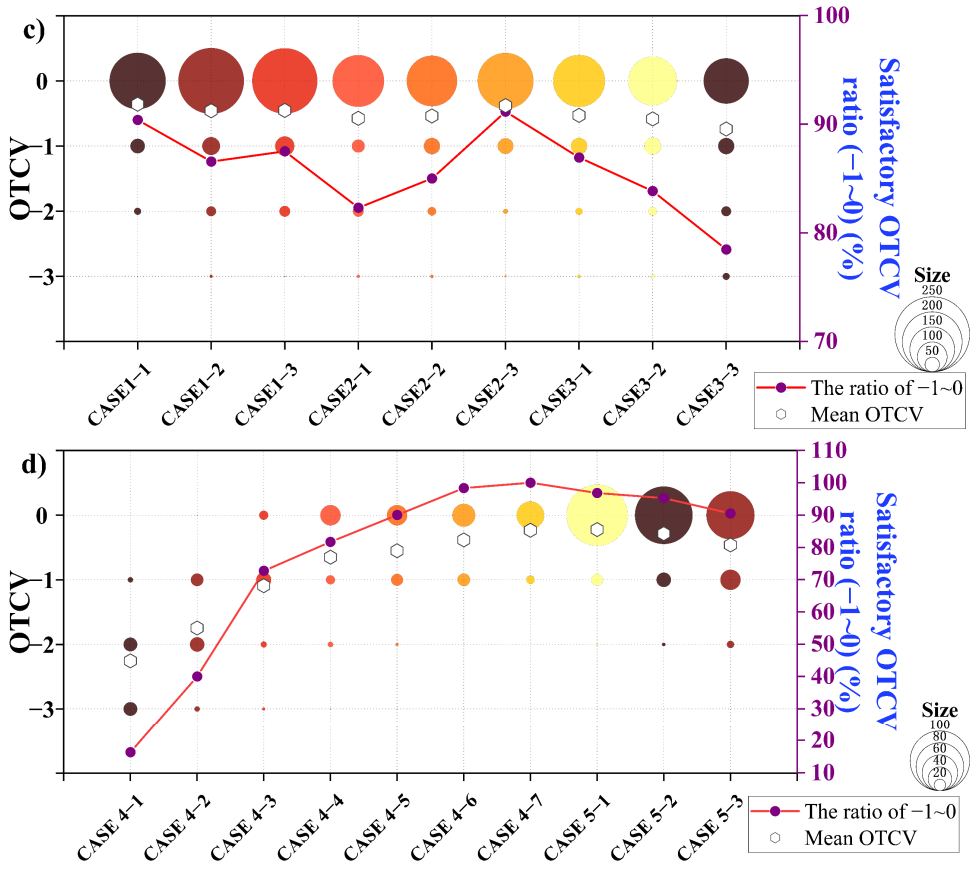


Figure 7. Subjective thermal evaluation distribution and satisfaction scores across different cases. (**a**,**c**) OTSV and OTCV distributions for intermittent heating cases; (**b**,**d**) OTSV and OTCV distributions for continuous heating cases.

3.3. Algorithm Results

3.3.1. Model Accuracy

Model accuracy is assessed via Equation (2). Figure 8 depicts the LR model's accuracy after adjusting various hyperparameters. The analysis indicates that the five solvers have a minimal effect on accuracy. In contrast, the C value (regularization coefficient) shows a steady rise, reaching a stable accuracy of 0.58 at values above 0.2.

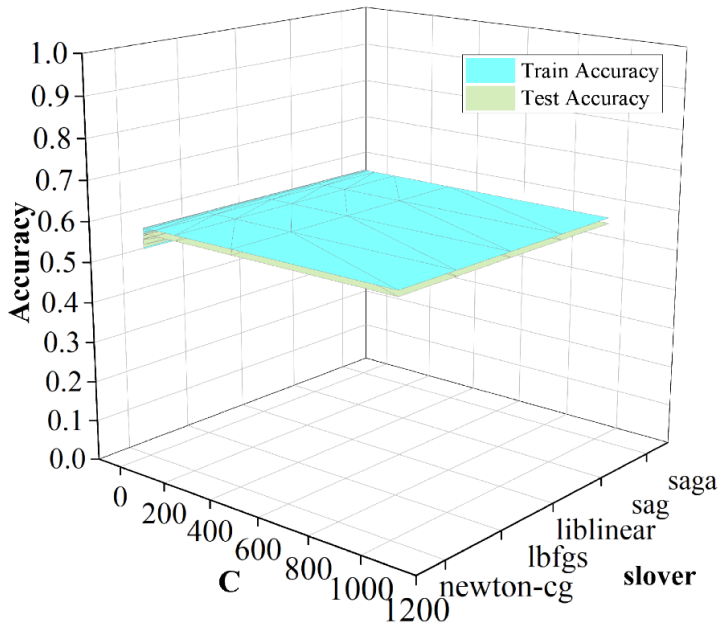


Figure 8. LR model accuracy.

Figure 9 illustrates the KNN model's accuracy. As the number of neighbors (N) rises, accuracy gradually decreases. This pattern may reflect the tendency of smaller N values to fit local detail more closely, which can lead to overfitting. This is confirmed by the gap between training and test accuracies, such as a 22% difference at N = 2 versus 9% at N = 10. The choice of distance calculation method also affects accuracy, with the Manhattan method producing the best results. Training set accuracy ranged from 0.69 to 0.85, while the test set accuracy was between 0.57 and 0.72.

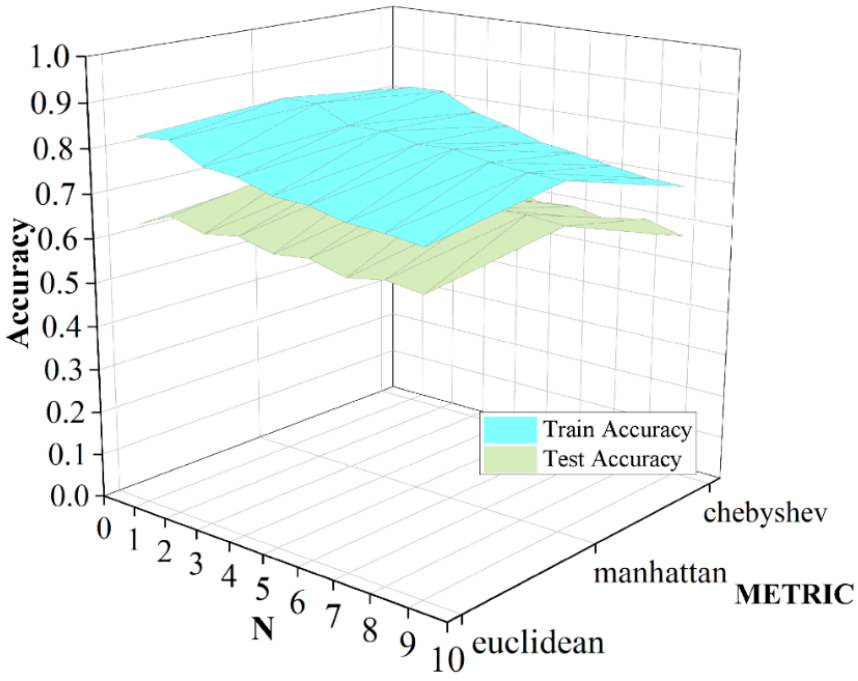


Figure 9. KNN model accuracy.

Figure 10 illustrates the SVM model accuracy, which ranges from 0.41 to 1.00 for the training set and from 0.41 to 0.71 for the test set. The C value in the SVM model positively affects training set accuracy, whereas test set accuracy first increases and then decreases as C increases, suggesting that excessively large C values may lead to overfitting. In our study, a C value over 1 yields training set accuracy above 0.98, indicating overfitting. The Gamma value in the Gaussian kernel also correlates positively with training set accuracy, with values above 1 potentially causing accuracy to exceed 0.98. For the test set, accuracy peaks at a Gamma value of 7.2 before decreasing.

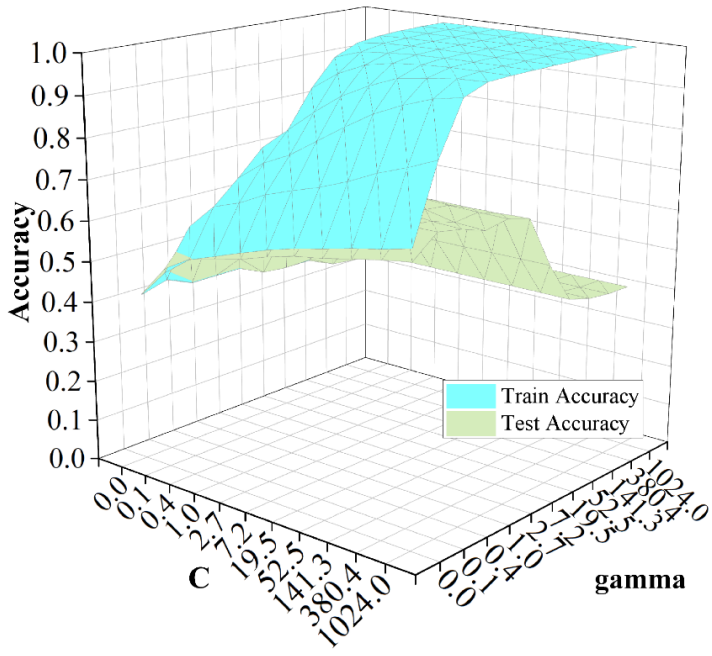


Figure 10. SVM model accuracy.

Figure 11 illustrates the RF model's accuracy. Notably, parameters such as min_samples_split, min_samples_leaf, and n_estimators have minimal impact on accuracy. These parameters contribute little to accuracy improvement while substantially increasing computational time. Conversely, the max_depth of each decision tree has a substantial influence on accuracy. As depth increased and data analysis became more granular, accuracy improved. The training set accuracy ranged from 0.58 to 1, while the test set accuracy varied from 0.56 to 0.86. Training set accuracy surpasses 90% when depth exceeds 10, while test set accuracy peaks at a depth of 11 and stabilizes around 0.82.

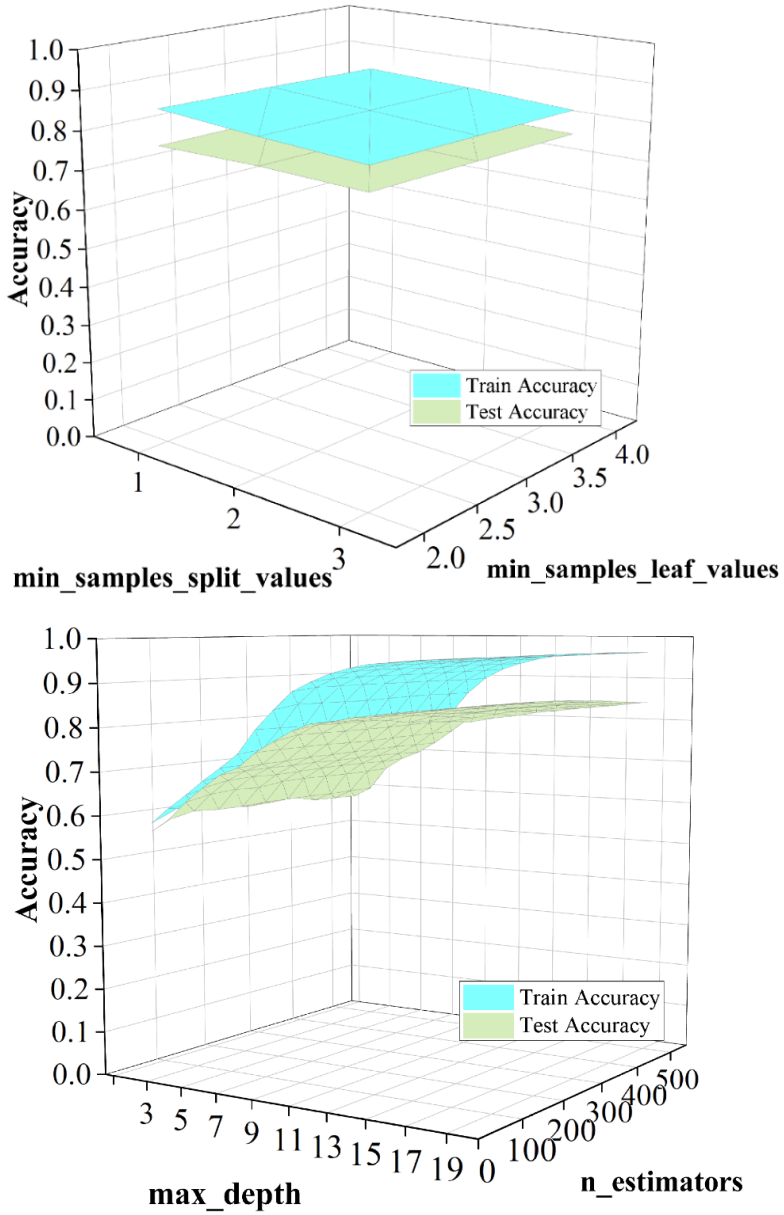


Figure 11. RF model accuracy.

Figure 12 depicts the ANN model's accuracy distribution across different hyperparameter settings. The regularized lambda and hidden layer neuron count have a negligible effect on accuracy, remaining stable between 0.5 and 0.6. In contrast, the output activation function and the number of hidden layers significantly impact accuracy. Using a logistic activation function reduces accuracy to 0.4. Additionally, changing the number of hidden layers does not alter accuracy when identity or logistic activation functions are used. When the Tanh activation function is used, relatively high accuracy is achieved with fewer hidden layers. However, when the number of hidden layers reaches four, the gap between the training and testing accuracies increases to 0.16, indicating a clear tendency toward overfitting. It should be noted that this phenomenon is observed only under this specific hyperparameter configuration and does not occur across all hyperparameter combinations.

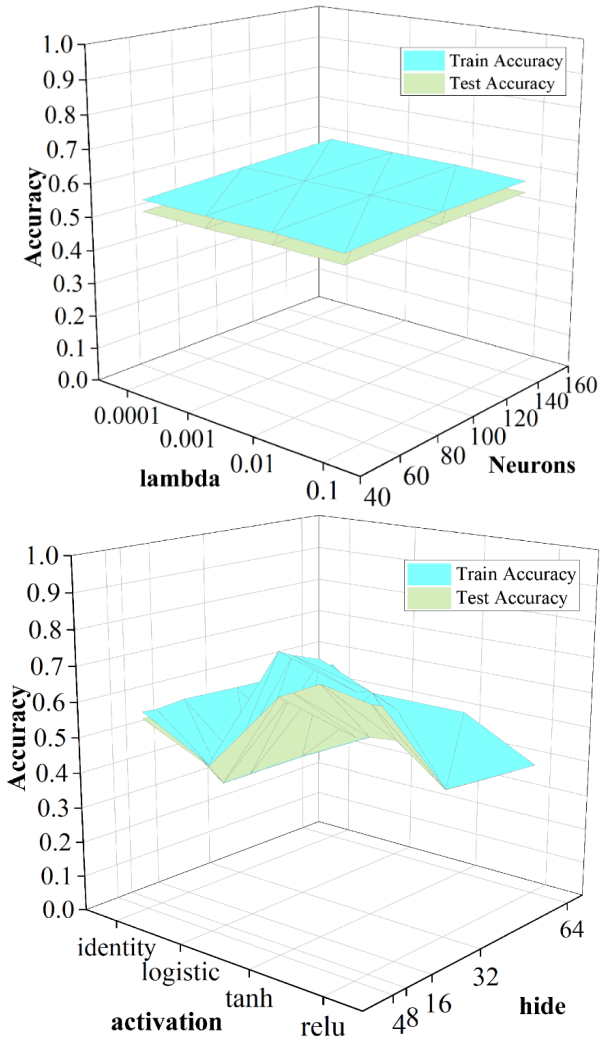


Figure 12. Accuracy of ANN model.

3.3.2. Determination of the Effective Model

The previous section examined the distribution of model accuracy under different hyperparameter settings and showed that the influence of primary and secondary parameters varies across models. Because a larger number of hyperparameters significantly increases the computational and analytical burden, parameters with negligible influence were excluded. The resulting set of retained hyperparameters is presented in Table 3. To identify the most stable and accurate hyperparameter combination, additional evaluation metrics—including recall and precision—were incorporated alongside accuracy to enable a more comprehensive assessment. The F1 score, which balances precision and recall and serves as a key evaluation metric, was calculated using Equations (3)–(5).

Table 3. Hyperparameters that primarily affect the model accuracy.

Algorithmic Models	Reserved Hyperparameters
LR	C
KNN	N, manhattan
SVM	C, gamma = 0.4
RF	Max_depth
ANN	Hide = 4, tanh

F1 score trends differ across models. Figure 13a shows the F1 scores of the LR model for each class in the training and test sets. F1 scores plateau and stabilize when the C value reaches 0.02. Scores range from 0.5 to 0.65, suggesting a moderate tradeoff between Recall and Precision. For the KNN model (Figure 13b), the number of neighbors (N value) shows minimal impact on F1 scores. Minimal differences are observed among the three classifications for both training and test sets. This suggests the KNN model effectively handles category imbalance in the three categorical variables. In addition, the F1 score of the training set is about 0.11 larger than that of the

test set on average. Coupled with Figure 8 results, this may indicate overfitting. A similar phenomenon is noted in the SVM model (Figure 13c). As the C value increases, the training set score reaches 0.98, while the test set score stabilizes at 0.7. For the RF model, the F1 score increases with the tree depth, as shown in Figure 13d. The disparity between training and test sets is smaller compared to other models. This indicates a better balance between recall and precision, leading to a lower classification error rate. For the ANN model (Figure 13e), the F1 score could not be calculated under some hyperparameter settings because certain classes had zero Precision or Recall, resulting in an undefined denominator in the F1 formulation. This phenomenon was associated with zero entries in parts of the confusion matrix, which may indicate sparse class predictions, class imbalance, or model bias toward dominant categories, rather than necessarily reflecting correct classification. Therefore, these cases were not interpreted as evidence of superior performance, but rather as a sign of unstable classification behavior under those parameter settings. Overall, the F1 scores on the training set ranged from 0.70 to 0.85, while those on the test set varied from 0.65 to 0.75.

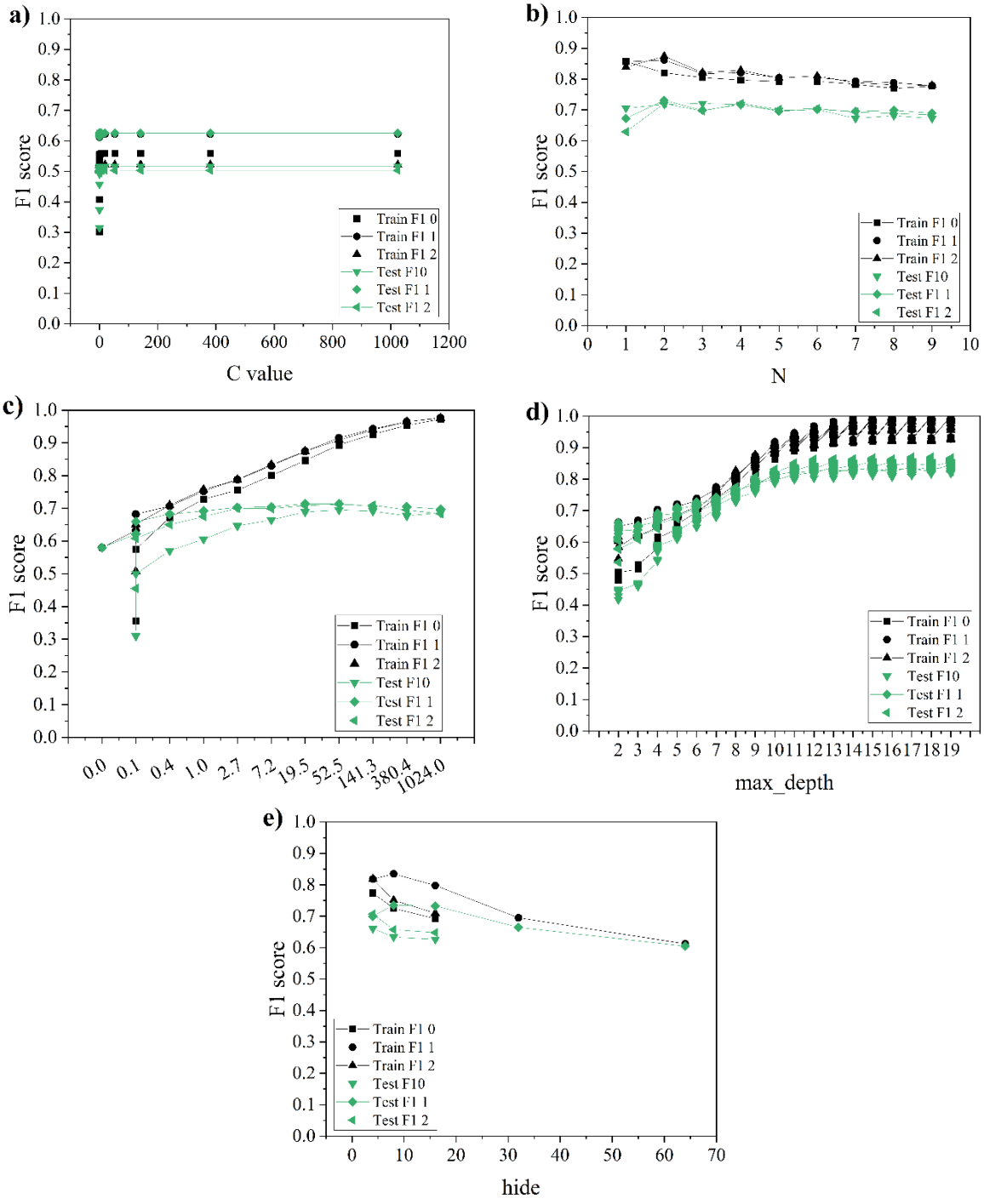


Figure 13. F1 score computed for the three categorical variables in five models. (**a**) LR; (**b**) KNN; (**c**) SVM; (**d**) RF; and (**e**) ANN.

In summary, under cross-validation across all five models, the LR and ANN models demonstrate lower accuracy and F1 scores for both training and test sets, indicating limited ability to capture patterns in the data. Conversely, the KNN and SVM exhibit instances where the accuracy of the training set surpasses that of the test set under certain combinations of hyperparameters, signifying a poor fit to new data. However, due to the limited sample size in this study, further analysis is challenging. Only the RF model exhibits good performance in both accuracy and F1 score. Its optimal hyperparameters are therefore analyzed further.

3.3.3. Optimal Parameters of the RF Model

The above analysis reveals that the RF model achieves improved accuracy and F1 scores at increased tree depths. However, a comparison shows that the gap between training and test set performances widens as max_depth approaches its maximum value. Thus, after excluding hyperparameter combinations for which the accuracy difference between the training and test sets exceeds 10%, the combination with the highest test set result is selected as the optimal solution. As demonstrated in Table 4, although min_samples_leaf and n_estimators have a negligible effect on model accuracy, a reduced min_samples_leaf leads to an increased number of splits, thereby elevating computational time. Similarly, higher n_estimators values lead to more decision trees, thereby extending overall computation time. Consequently, the optimal RF model configuration includes a max_depth of 13, min_samples_split of 2, min_samples_leaf of 4, and n_estimators of 150, achieving a model accuracy of 0.84.

The confusion matrix constructed using this optimal hyperparameter combination (Figure 14) further validates its effectiveness, showing strong and well-balanced classification performance. F1 scores for all three classes range from 0.83 to 0.85, while both macro-average and weighted-average F1 scores are close to 0.845, indicating consistently strong classification capability across all categories. The recall rates for categories 0, 1, and 2 are approximately 81%, 83%, and 90%, respectively, while the corresponding precision rates are 87%, 85%, and 81%. This indicates that the model effectively identifies most true samples across different thermal states, demonstrating both high classification reliability and completeness.

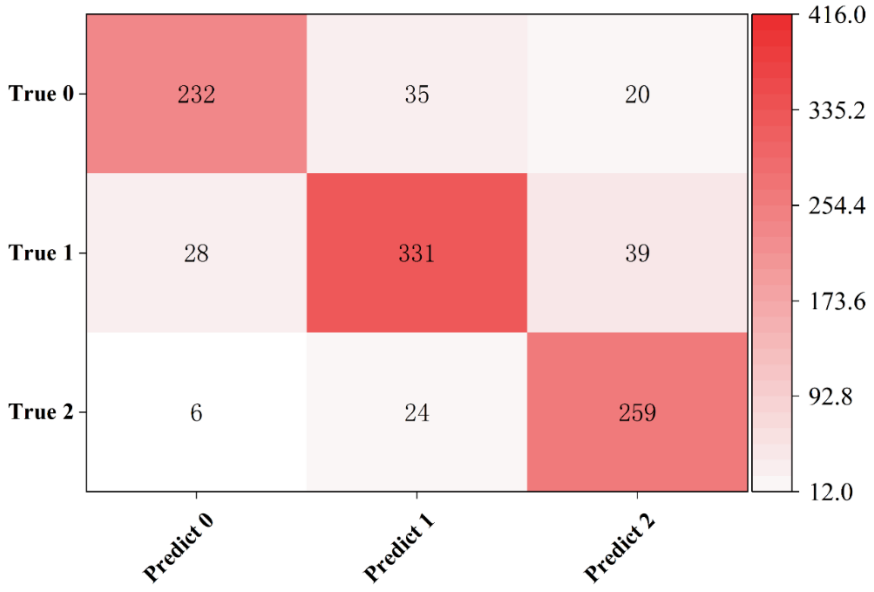


Figure 14. Confusion matrix of the RF model with the optimal hyperparameter combination.

Table 4. Optimal hyperparameter combinations for RF model.

max_depth	min_samples_split	min_samples_leaf	n_estimators	Train Accuracy	Test Accuracy	Δ
13	2	2	150	0.94	0.84	9.97
13	2	2	300	0.94	0.84	9.94
13	2	3	150	0.94	0.84	9.97
13	2	3	300	0.94	0.84	9.94
13	2	4	150	0.94	0.84	9.97
13	2	4	300	0.94	0.84	9.94

To assess the optimal model's generalization capability, its ROC curve and AUC metrics were evaluated, with results presented in Figure 15. The ROC curve's deviation from the diagonal line reflects the model's performance; a greater deviation indicates superior performance. AUC, representing the area under the ROC curve, signifies the model's capacity to distinguish between classifications, with values closer to 1 indicating more accurate classifications. With AUC values of 0.96, 0.93, and 0.95 for classifications 0, 1, and 2 respectively, the model demonstrates exceptional performance and generalization capabilities.

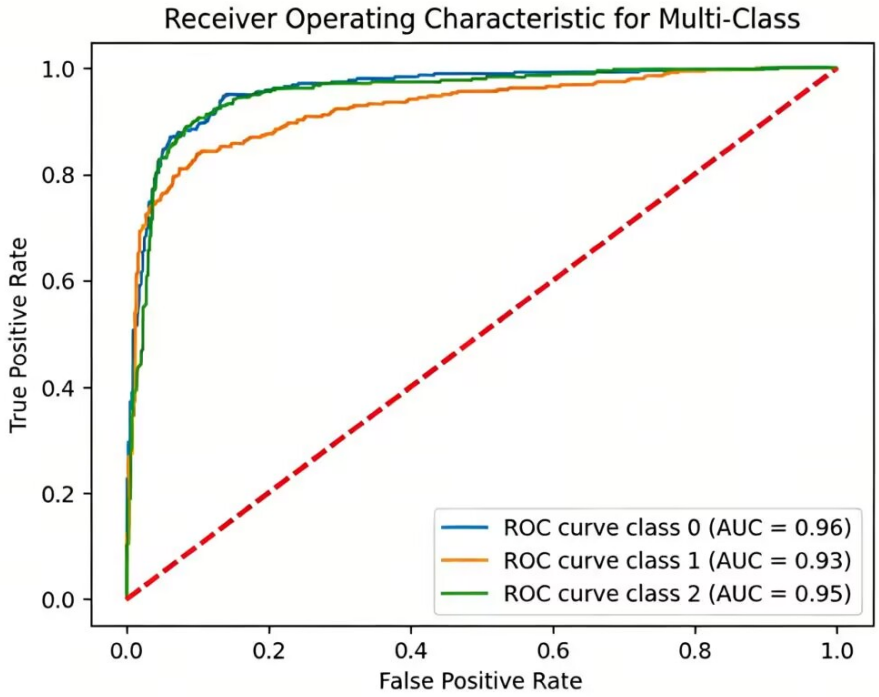


Figure 15. ROC curves of the optimized RF model.

3.4. Limitations and Future Work

This study systematically investigated the spatiotemporal dynamic heating strategy of a catalytic combustion localized heater. Although the results offer both theoretical insight and practical implications, several limitations should be noted. First, the participants were restricted to a physiologically homogeneous group of healthy young adults, excluding cold-sensitive populations such as older adults, children, and patients, despite known age- and physiology-related differences in thermal comfort and thermoregulatory capacity. Second, while the environmental conditions were designed to reflect typical outdoor scenarios, the influences of climatic variability, particularly differences in humidity and wind speed across regions, on infrared radiant heat transfer and human thermal responses were not considered. Third, the continuous and intermittent heating experiments were conducted under short-term exposure conditions of 60–75 min, and the conclusions are therefore mainly applicable to thermal responses within this time scale. Thermal comfort responses and appropriate control strategies under real outdoor conditions involving either brief stays or prolonged exposure remain to be further explored. Finally, although the proposed spatiotemporal dynamic heating strategy was demonstrated to be feasible under the tested conditions, additional validation and optimization of model parameters and control thresholds are still required under different environmental conditions and datasets to support wider application in localized heating practice.

4. Conclusions

This study established a feasible heating strategy framework and predictive model based on skin temperature and subjective thermal response data collected from localized PCS heating systems under various operating conditions. The main findings are summarized as follows:

(1) Localized heating effectively mitigates cold discomfort. Under continuous heating, reducing the heating distance from 80 cm to 40 cm resulted in an approximate 0.4 °C increase in MST. Intermittent heating maintains MST within the range of 30–33 °C while reducing energy consumption.

(2) In intermittent heating mode, OTSV satisfaction remains high (72%), and the long-distance intermittent heating strategy demonstrates both strong thermal comfort performance and energy-saving potential. Appropriately

increasing the heating distance helps regulate thermal sensation within the defined target comfort interval. In continuous heating mode, when $T_{in} > 0$ °C, OTSV satisfaction reached an average of 65%.

(3) This study builds upon existing heating control frameworks by introducing a machine learning–based dynamic adaptive heating strategy. This approach reduces reliance on detailed physical modelling of local heat transfer mechanisms while strengthening the relationship between diverse environmental conditions and subjective thermal responses. Based on the defined comfort interval (OTSV = [−1, 0]), an adaptive predictive framework and model for thermal comfort under infrared localized heating were established.

(4) Model performance evaluation indicates that, among the five machine learning algorithms compared, the Random Forest (RF) model achieved the best performance in thermal state prediction. After hyperparameter optimization, the model achieved an accuracy of 0.84. It also demonstrated strong classification capability in the three-class OTSV evaluation, with F1 score, recall, and precision all exceeding 80%. ROC curve analysis further showed that the AUC values for all three classes exceeded 0.93, indicating excellent generalization capability.

This study provides a practical intelligent control strategy for catalytic combustion infrared heaters and establishes a design foundation for low-energy, comfort-oriented personalized thermal environment systems in cold outdoor work environments. By enabling individualized thermal comfort regulation in outdoor settings and reducing reliance on full-space heating, it further offers useful implications for enhancing urban resilience in cold climates and for supporting energy-efficient building environmental design.

Author Contributions

H.F.: writing—original draft preparation, data curation, visualization; J.J.: writing—original draft preparation, data curation, visualization; M.Q.: writing—original draft preparation, review and editing, conceptualization, methodology, supervision; X.H., Y.Y., and S.S.: writing—review and editing, methodology. All authors have read and agreed to the published version of the manuscript.

Funding

This work was supported by the Talent Introduction Program of Xihua University (Grant No. ZX20250024).

Institutional Review Board Statement

Not applicable. Ethical review and approval were waived for this study, as it only involves the retrospective analysis of existing experimental data collected over multiple years. This study focuses on data-driven modeling and relevant data analysis, with no direct human intervention or involvement of identifiable private information.

Informed Consent Statement

Not applicable.

Data Availability Statement

The data supporting the findings of this study are included within the article.

Conflicts of Interest

The authors declare no conflict of interest.

Use of AI and AI-Assisted Technologies

No AI tools were utilized for this paper.

References

1. Zhan, H.X.; Lin, G. Roof-Integrated Phase Change Materials for Urban Heat Island Mitigation: Advances and Strategies. *Int. J. Environ. Sci. Technol.* **2026**, *23*, 301. https://doi.org/10.1007/s13762-026-07108-1.
2. Mohtasham, D. Several Fans Treated for Hypothermia at the Fourth-Coldest Game in NFL History. Available online: https://www.npr.org/2024/01/17/1225209300/chiefs-dolphins-hypothermia-cold (accessed on 11 December 2025).
3. Kamata, H.; Seto, S.; Suppasri, A.; et al. A Study on Hypothermia and Associated Countermeasures in Tsunami Disasters: A Case Study of Miyagi Prefecture during the 2011 Great East Japan Earthquake. *Int. J. Disaster Risk Reduct.* **2022**, *81*, 103253. https://doi.org/10.1016/j.ijdrr.2022.103253.

4. Qin, M.Y.; Chew, B.T.; Yau, Y.H.; et al. A Novel Evaluation Indicator and Optimal Heating Strategy for Using an Intermittent-Operation Catalytic Combustion Heater in Open Cold Environments. *Build. Environ.* **2024**, *252*, 111271. https://doi.org/10.1016/j.buildenv.2024.111271.
5. Hu, J.H.; Li, Z.W.; Zhu, J.L.; et al. Effect of Compound Exposure to Snowstorm and Cold Spell on Acute Myocardial Infarction Mortality. *Environ. Res.* **2025**, *272*, 121191. https://doi.org/10.1016/j.envres.2025.121191.
6. Wu, J.S.; Hu, Z.Q.; Han, Z.X.; et al. Human Physiological Responses of Exposure to Extremely Cold Environments. *J. Therm. Biol.* **2021**, *98*, 102933. https://doi.org/10.1016/j.jtherbio.2021.102933.
7. Wu, J.S.; Sun, B.Y.; Hu, Z.Q.; et al. Physiological Responses and Thermal Sensation during Extremely Cold Exposure (−20 °C). *Build. Environ.* **2021**, *206*, 108338. https://doi.org/10.1016/j.buildenv.2021.108338.
8. Kim, K.; Stephens, K.K.; McGlone, M.S.; et al. Strengthening Individual Preparedness for Extreme Cold Weather through Enhanced Messaging, Risk Perception, and Trust. *Sustain. Cities Soc.* **2025**, *121*, 106164. https://doi.org/10.1016/j.scs.2025.106164.
9. Huang, X.Z.; Yao, R.M.; Xu, T.T.; et al. The Impact of Heatwaves on Human Perceived Thermal Comfort and Thermal Resilience Potential in Urban Public Open Spaces. *Build. Environ.* **2023**, *242*, 110586. https://doi.org/10.1016/j.buildenv.2023.110586.
10. Liu, C.; Tang, Y.Z.; Sun, L.M.; et al. Effects of Local Heating of Body on Human Thermal Sensation and Thermal Comfort. *J. Build. Eng.* **2022**, *53*, 104543. https://doi.org/10.1016/j.jobe.2022.104543.
11. Wang, J.H.; Ju, X.Y.; Wang, M.; et al. Alternating Intermittent Heating: An Energy-Efficient Wearable Heating Strategy for Enhanced Comfort in Extremely Cold Environments. *Energy* **2025**, *339*, 139010. https://doi.org/10.1016/j.energy.2025.139010.
12. Kaczmarczyk, J.; Melikov, A.; Sliva, D. Effect of Warm Air Supplied Facially on Occupants' Comfort. *Build. Environ.* **2010**, *45*, 848–855. https://doi.org/10.1016/j.buildenv.2009.09.005.
13. Du, C.Q.; Liu, H.; Li, C.J.; et al. Demand and Efficiency Evaluations of Local Convective Heating to Human Feet and Low Body Parts in Cold Environments. *Build. Environ.* **2020**, *171*, 106662. https://doi.org/10.1016/j.buildenv.2020.106662.
14. Wang, H.Y.; Wang, J.; Li, W.Y.; et al. Experimental Study on a Radiant Leg Warmer to Improve Thermal Comfort of Office Workers in Winter. *Build. Environ.* **2022**, *207*, 108461. https://doi.org/10.1016/j.buildenv.2021.108461.
15. Wang, T.Y.; Wang, H.C.; Luo, Z.W. Effects of Local Heating of Phase Change Floor (PCF) on Thermal Comfort and Energy Efficiency. *J. Build. Eng.* **2025**, *103*, 112157. https://doi.org/10.1016/j.jobe.2025.112157.
16. Asai, M.; Fukasawa, R.; Matsui, T. Heat Transfer Controlling the Temperature of Human Forehead at Rest and during Walking. *Int. J. Heat Mass Transfer* **2026**, *256*, 128025. https://doi.org/10.1016/j.ijheatmasstransfer.2025.128025.
17. Cheng, Z.Q.; Xu, J.X.; Lu, Y.H. A Multi-Scale Simulation for Heat Transfer between Human and Heated Clothing: Towards Personalized and Efficient Thermal Management. *Build. Environ.* **2026**, *287*, 113764. https://doi.org/10.1016/j.buildenv.2025.113764.
18. Fanger, P.O. Assessment of Man's Thermal Comfort in Practice. *Occup. Environ. Med.* **1973**, *30*, 313–324.
19. Choi, J.-H.; Yeom, D. Study of Data-Driven Thermal Sensation Prediction Model as a Function of Local Body Skin Temperatures in a Built Environment. *Build. Environ.* **2017**, *121*, 130–147. https://doi.org/10.1016/j.buildenv.2017.05.004.
20. Yang, B.; Li, X.J.; Liu, Y.H.; et al. Comparison of Models for Predicting Winter Individual Thermal Comfort Based on Machine Learning Algorithms. *Build. Environ.* **2022**, *215*, 108970. https://doi.org/10.1016/j.buildenv.2022.108970.
21. Zhou, X.; Xu, L.; Zhang, J.S.; et al. Data-Driven Thermal Comfort Model via Support Vector Machine Algorithms: Insights from ASHRAE RP-884 Database. *Energy Build.* **2020**, *211*, 109795. https://doi.org/10.1016/j.enbuild.2020.109795.
22. Cai, S.H.; Gou, Z.H. Spatiotemporal Prediction of Thermal Comfort in Open-Plan Offices: A Data-Efficient Framework Integrating Machine Learning and Modified PMV_{st} Model. *Build. Environ.* **2026**, *290*, 114167. https://doi.org/10.1016/j.buildenv.2025.114167.
23. Huang, W.H.; Tan, G.S.; Zhao, B.L.; et al. A Data-Driven Framework for Developing Virtual Personal Comfort Models: Integrating Thermal Sensitivity and Preference Prediction via Supervised Learning. *Case Stud. Therm. Eng.* **2025**, *75*, 107160. https://doi.org/10.1016/j.csite.2025.107160.
24. Ren, Z.L.; Gao, X.K.; Xiao, Y.M.; et al. Thermal Comfort and Energy Conservation of a Four-Sided Enclosed Local Heating Device in a Cold Environment. *Build. Environ.* **2023**, *228*, 109837. https://doi.org/10.1016/j.buildenv.2022.109837.
25. *GB/T 18883-2022*; Standard for Indoor Air Quality. State Administration for Market Regulation and National Standardization Administration: Beijing, China, 2022.
26. Qin, M.Y.; Chew, B.T.; Yau, Y.H.; et al. Emergency Heater Based on Gas-Fired Catalytic Combustion Infrared Technology: Structure, Evaluation and Thermal Response. *Energy* **2023**, *274*, 127426. https://doi.org/10.1016/j.energy.2023.127426.
27. *ASHRAE 55-2023*; *Thermal Environmental Conditions for Human Occupancy*; American Society of Heating, Refrigerating and Air-Conditioning Engineers: Atlanta, GA, USA, 2023.
28. Kurazumi, Y.; Horikoshi, T.; Tsuchikawa, T.; et al. The Body Surface Area of Japanese. *JPN J. Biometeorol.* **1994**, *31*, 5–29. https://doi.org/10.11227/seikisho1966.31.5.

29. Cao, W.; Xuan, X.D.; Wang, Y.C.; et al. The Thermal Sensitivity (Griffiths Constant) of Occupants for Naturally Ventilated Buildings in China. *Energy Build.* **2025**, *341*, 115786. https://doi.org/10.1016/j.enbuild.2025.115786.
30. Yang, Z.X.; Dong, X.; Xiao, H.S.; et al. Investigation of Thermal Comfort of Room Air Conditioner during Heating Season. *Build. Environ.* **2022**, *207*, 108544. https://doi.org/10.1016/j.buildenv.2021.108544.
31. Qin, M.Y.; Chew, B.T.; Yau, Y.H.; et al. Thermal Comfort Characteristics of a Catalytic Combustion Heater under Wind-Chilled Exposure. *J. Clean. Prod.* **2024**, *436*, 140701. https://doi.org/10.1016/j.jclepro.2024.140701.
32. Pasha, S.J.; Mohamed, E.S. Advanced Hybrid Ensemble Gain Ratio Feature Selection Model Using Machine Learning for Enhanced Disease Risk Prediction. *Inform. Med. Unlocked* **2022**, *32*, 101064. https://doi.org/10.1016/j.imu.2022.101064.
33. Derczynski, L. Complementarity, F-score, and NLP Evaluation. In Proceedings of the Tenth International Conference on Language Resources and Evaluation (LREC'16), Portorož, Slovenia, 23–28 May 2016; pp. 261–266.
34. Li, S.Y.; Xu, J.; Liu, W.W.; et al. Comparison of the Performance of Local Skin Temperatures in Evaluating Overall Thermal Comfort at Normal Room Temperatures. *Build. Environ.* **2025**, *267*, 112296. https://doi.org/10.1016/j.buildenv.2024.112296.